Title

Impact of Changing Winds on the Mauna Loa CO2 Seasonal Cycle in Relation to the Pacific Decadal Oscillation

Journal

Journal of Geophysical Research: Atmospheres, 127(13)

ISSN

2169-897X

Authors

Jin, Yuming
Keeling, Ralph F
Rödenbeck, Christian
et al.

Publication Date

2022-07-16

DOI

10.1029/2021jd035892

Peer reviewed

JGR Atmospheres

RESEARCH ARTICLE
10.1029/2021JD035892

Impact of Changing Winds on the Mauna Loa CO_2 Seasonal Cycle in Relation to the Pacific Decadal Oscillation

Yuming Jin[1], Ralph F. Keeling[1], Christian Rödenbeck[2], Prabir K. Patra[3], Stephen C. Piper[1], and Armin Schwartzman[4]

[1]Scripps Institution of Oceanography, University of California, San Diego, La Jolla, CA, USA, [2]Max Planck Institute for Biogeochemistry, Jena, Germany, [3]Research Institute for Global Change, Japan Agency for Marine-Earth Science and Technology, Yokohama, Japan, [4]Division of Biostatistics, Halıcıoğlu Data Science Institute, University of California, San Diego, La Jolla, CA, USA

Abstract Long-term measurements at the Mauna Loa Observatory (MLO) show that the CO_2 seasonal cycle amplitude (SCA) increased from 1959 to 2019 at an overall rate of 0.22 ± 0.034 ppm decade^{-1} while also varying on interannual to decadal time scales. These SCA changes are a signature of changes in land ecological CO_2 fluxes as well as shifting winds. Simulations with the TM3 tracer transport model and CO_2 fluxes from the Jena CarboScope CO_2 Inversion suggest that shifting winds alone have contributed to a decrease in SCA of -0.10 ± 0.022 ppm decade^{-1} from 1959 to 2019, partly offsetting the observed long-term SCA increase associated with enhanced ecosystem net primary production. According to these simulations and MIROC-ACTM simulations, the shorter-term variability of MLO SCA is nearly equally driven by varying ecological CO_2 fluxes (49%) and varying winds (51%). We also show that the MLO SCA is strongly correlated with the Pacific Decadal Oscillation (PDO) due to varying winds, as well as with a closely related wind index (U-PDO). Since 1980, 44% of the wind-driven SCA decrease has been tied to a secular trend in the U-PDO, which is associated with a progressive weakening of westerly winds at 700 mbar over the central Pacific from 20°N to 40°N. Similar impacts of varying winds on the SCA are seen in simulations at other low-latitude Pacific stations, illustrating the difficulty of constraining trend and variability of land CO_2 fluxes using observations from low latitudes due to the complexity of circulation changes.

Plain Language Summary The CO_2 seasonal amplitude is an indicator of the growing-season productivity of land ecosystems. CO_2 observation at Mauna Loa Observatory (MLO) showed an increasing amplitude from 1959 to 2019, probably due to significantly enhanced productivity over the Eurasia temperate and boreal forest. In this study, we show that about a third of this observed amplitude increase at MLO was offset by long-term circulation changes, which isolated the air at low latitudes from the influence of northern high-latitude ecosystems. This wind-driven impact is also important at other low-latitude Pacific stations. The CO_2 seasonal amplitude at MLO also has considerable short-term variability (on the scale of multiple years to decades), roughly half of which is regulated by the changing winds, while the remaining half is driven by the variability of ecological CO_2 fluxes. We show that the wind influence is closely associated with a climate index known as the Pacific Decadal Oscillation. Our study indicates that the attribution of amplitude changes at low-latitudes stations to ecosystem changes is complicated by wind shifts.

Key Points:

- The increasing CO_2 seasonal amplitude observed at the Mauna Loa Observatory since 1959 has been significantly offset by circulation changes
- Variability of CO_2 seasonal cycles at Mauna Loa is partly regulated by circulation changes associated with the Pacific Decadal Oscillation
- Circulation changes complicate using low-latitudes CO_2 observation to constrain changing land carbon cycle

Supporting Information:

Supporting Information may be found in the online version of this article.

Correspondence to:

Y. Jin,
y2jin@ucsd.edu

Citation:

Jin, Y., Keeling, R. F., Rödenbeck, C., Patra, P. K., Piper, S. C., & Schwartzman, A. (2022). Impact of changing winds on the Mauna Loa CO_2 seasonal cycle in relation to the Pacific Decadal Oscillation. *Journal of Geophysical Research: Atmospheres*, *127*, e2021JD035892. https://doi.org/10.1029/2021JD035892

Received 22 SEP 2021
Accepted 16 JUN 2022

Author Contributions:

Conceptualization: Yuming Jin, Ralph F. Keeling, Stephen C. Piper
Data curation: Yuming Jin
Formal analysis: Yuming Jin
Funding acquisition: Ralph F. Keeling
Investigation: Yuming Jin
Methodology: Yuming Jin, Ralph F. Keeling, Armin Schwartzman
Project Administration: Ralph F. Keeling

1. Introduction

In the Northern Hemisphere, the concentration of CO_2 at remote atmospheric stations undergoes a clear seasonal cycle driven mostly by CO_2 uptake and release from the land biosphere (Keeling, 1960; Randerson et al., 1997) as modulated by atmospheric mixing. Since the early 1960s, an increase in the CO_2 seasonal cycle amplitude (SCA) has been observed at surface stations and airborne transects, with a larger relative increase at higher latitudes (Forkel et al., 2016; Graven et al., 2013). At Mauna Loa (MLO, 19.5°N), a ~15% increase has been observed from 1959 to the early 2010s, while at northern high-latitude station Barrow (BRW, 71.3°N), the increase of the same time period is ~35% (Graven et al., 2013). These long-term amplitude trends (henceforth "trend") are superimposed on considerable interannual to decadal variability (henceforth "variability"; Keeling et al., 1996). For example, at MLO, as shown in Figure 1a, the amplitude was relatively constant from 1960 to 1970, and grew by 15% over the 1970s, but then increased by only 5% from 1980 to 2020 with considerable interannual variability.

Resources: Yuming Jin, Ralph F. Keeling, Christian Rödenbeck, Prabir K. Patra
Software: Yuming Jin, Christian Rödenbeck, Prabir K. Patra
Supervision: Ralph F. Keeling
Validation: Yuming Jin
Visualization: Yuming Jin
Writing – original draft: Yuming Jin
Writing – review & editing: Yuming Jin, Ralph F. Keeling, Christian Rödenbeck, Prabir K. Patra, Stephen C. Piper, Armin Schwartzman

The SCA increase is an important indicator of enhanced growing-season ecosystem productivity over the northern temperate and boreal forest (Graven et al., 2013; Lin et al., 2020). Increasing SCA has been used as an emergent constraint on CO_2 fertilization of primary production (Wenzel et al., 2016), which is possible because simulations from land ecosystem models that are coupled with atmospheric transport models attribute much of the simulated SCA increase to CO_2 fertilization (Bastos et al., 2019; Ito et al., 2016; Piao et al., 2018; Zhao et al., 2016). However, most of these coupled models systematically underestimate the SCA increase at high latitudes and in the midtroposphere (500 mbar) from 1960 to 2010, suggesting that the ecosystem models are missing key mechanisms (Graven et al., 2013; Thomas et al., 2016). Possibilities include underestimating CO_2 fertilization on light-use efficiency (Haverd et al., 2020; Thomas et al., 2016), or underestimating response of changing land carbon cycle to climate change. Early studies which examined SCA changes up until the mid-1990s attributed the SCA increase to enhanced photosynthetic CO_2 uptake due to warming-induced lengthening of the growing season, especially in spring (Keeling et al., 1996; Randerson et al., 1999). In contrast, recent studies focusing on trends after 1990 suggest that the CO_2 uptake has become increasingly limited by water stress tied to continued warming (Jiao et al., 2021; Lian et al., 2020; Peñuelas et al., 2017; Wang et al., 2018; Zhang et al., 2020). The SCA trend has likely also been strongly influenced by warming-driven changes in vegetation cover (Forkel et al., 2016; Liu et al., 2020), and changes in agriculture and other land-use changes (Gray et al., 2014; Zeng et al., 2014). Interannual to decadal climate change, including soil temperature and water supply availability, has been suggested as a major source of SCA variability (Buermann et al., 2007).

Our ability to infer changes in growing-season productivity or constrain CO_2 fertilization from changes in SCA may be complicated, however, by variations in atmospheric circulation. Taguchi et al. (2003) and Lintner et al. (2006) found that the MLO SCA is sensitive to the interannual variations in the airflow from Siberia, where the biospheric CO_2 signal is especially strong. Murayama et al. (2007) found significant year-to-year variabilities of the seasonal cycle at two high-latitude stations (BRW and Alert) caused by changing atmospheric circulation alone. Higuchi et al. (2002) showed that atmospheric transport alone produced significant variations in SCA on interannual to quasi-decadal time scales at both MLO and at high-latitude station BRW. Wang et al. (2020) showed that, since 1959, MLO has become more influenced by CO_2 exchanges from Amazonia, which could be connected with an expansion of the Hadley cell in the Southern Hemisphere. These studies, which explore the connection between SCA changes and atmospheric circulation, however, did not discuss connections between decadal climate modes and wind influences on SCA, and did not discuss possible impacts of long-term wind shifts within the Northern Hemisphere.

Here we study the contribution of varying winds and varying ecological CO_2 fluxes to the trend and variability of SCA, using surface-to-atmosphere CO_2 fluxes transported by the Atmospheric Tracer Model 3 (TM3, Heimann & Körner, 2003), and the MIROC4.0-based Atmospheric Chemistry-Transport Model (ACTM, Patra et al., 2018). We focus primarily on impacts at MLO, but also briefly examine impacts on other low-latitude stations as well as high-latitude station BRW. For MLO, we examine the correlation between MLO SCA and several climate indices, including the Pacific Decadal Oscillation (PDO; Mantua et al., 1997), a closely related wind index U-PDO (based on the first EOF of subtropical 700 mbar winds), land temperature and Palmer Drought Severity Index (PDSI). We also examine MLO 10-day back trajectories under different phases of the PDO to better understand transport pathways. We discuss these results in connection with changes in MLO SCA variability and circulation changes on the interannual to decadal scale and the long-term trend. The results highlight the significant role of changing circulation on the variability and SCA trend at MLO as well as other low-latitude stations, which complicates using SCA at these stations to quantify large-scale ecological changes (e.g., Wenzel et al., 2016).

2. Data and Methods

2.1. CO_2 Observation and Its SCA

We use monthly averaged atmospheric in situ CO_2 measurements at MLO, from the Scripps CO_2 Program (Keeling et al., 2001). All the missing values from February to April in 1964 are filled by linear interpolation. We compute the SCA by using the Thoning function following the steps below (Thoning et al., 1989):

1. Fit the observed MLO SCA with a cubic polynomial for the trend and 4-harmonics for the climatological seasonal cycle (Equation 1).

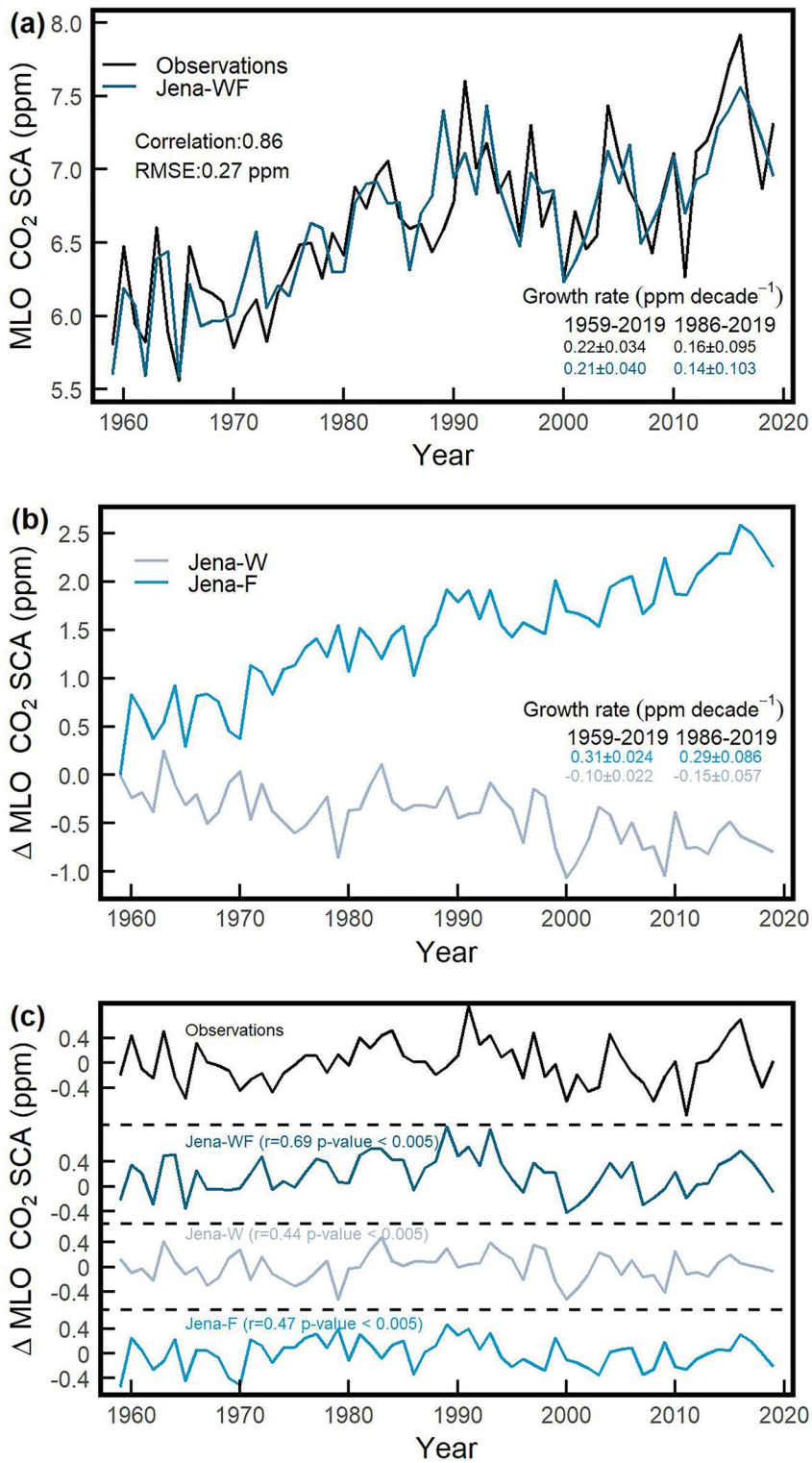

Figure 1. (a) Observed Mauna Loa Observatory (MLO) seasonal cycle amplitude (SCA) and modeled MLO SCA from Jena-WF. The Jena-WF simulation is scaled down by 5% since it systematically overestimates the SCA. (b) Anomalies (reference year 1959) of MLO SCA components simulated by Jena-W and Jena-F. Each simulation is scaled down by 5%. The growth rates in (a) and (b) are computed by generalized least-square (GLS) method (see Section 2.1), from 1959 to 2019, and from 1986 to 2019. (c) Anomalies of detrended MLO SCA, simulated and detrended MLO SCA from Jena-WF, Jena-W, and Jena-F. Each time series is detrended by removing its long-term linear trend. We also show the correlation (r) between each detrended simulation and detrended observations, and the corresponding p-value based on 1,000 iterations of two-tailed random phase test of each correlation (Ebisuzaki, 1997).

$$CO_2(t) = \sum_{i=0}^{i=3} a_i t^i + \sum_{j=1}^{j=4} [b_i \sin(2j\pi t) + c_i \cos(2j\pi t)] + \sigma(t) \quad (1)$$

where t is the decimal year; a_i are the coefficients for the long-term trend; b_j and c_j are the coefficients for the climatological seasonal cycle; and $\sigma(t)$ is the residual term.

2. Apply a Butterworth band-pass filter to the residual ($\sigma(t)$) with 90-day and 540-day cutoffs.
3. Compute the seasonal amplitude of the sum of the harmonic and band-passed residual, using the peak and trough values for each calendar year.

We note that our choice of parameters is slightly different compared to the default setup of the Thoning function, but the impact on calculated SCA is negligibly small with RMSE of 0.023 ppm from 1959 to 2019. We then compute the long-term growth rate (ppm decade^{-1}) of CO_2 SCA using generalized least-square (GLS) regression (Fox & Weisberg, 2019; Pinheiro et al., 2021). We choose this method in order to address serial correlation, as we find significant first-order autocorrelation of the SCA time series suggested by partial autocorrelation function.

2.2. Modeled MLO CO_2 Seasonal Cycle

We simulate CO_2 concentrations at MLO using two models. The first model is the global Atmospheric Tracer Model 3 (TM3; Heimann & Körner, 2003), which was run at 5° in longitude and 4° in latitude with 19 vertical levels, using 6-hourly NCEP/NCAR reanalysis meteorological fields (Kalnay et al., 1996) from 1951 to 2019, and surface fluxes from the Jena CarboScope CO_2 Inversion (version ID: s57Xoc_v2020, Rödenbeck et al., 2003, 2018). The first six years (1951–1956) are model spin-up period. The inversion only uses available CO_2 observations from four stations (MLO, BRW, La Jolla, and South Pole) over the period of 1958–2019. We use two TM3 simulations: one driven by year-to-year variations in both winds and fluxes (Jena-WF), and one driven by year-to-year varying winds but climatological average cyclostationary fluxes from 1957 to 2019 (Jena-W). The difference between Jena-WF and Jena-W is referred to as Jena-F, which can approximate the impact of varying ecological CO_2 fluxes alone on the variability and trend of MLO SCA. On average, Jena-WF overestimates the MLO SCA by 5% compared to the observation. To correct for this systematic offset, we scale these simulated SCA (Jena-WF, Jena-W, and Jena-F) down by 5%. This correction only has a small impact on our analysis, since we primarily focus on the SCA variability relative to each other, and the long-term SCA trend.

In order to account for uncertainties of the transport model and reanalysis wind fields, we also simulate CO_2 with MIRCO-ACTM (Patra et al., 2005, 2018). The ACTM model was run at ~2.8° in longitude and ~2.8° in latitude with 67 vertical levels driven by JRA-55 winds (Kobayashi et al., 2015) from 1981 to 2019, with the first four years (1981–1984) as model spin-up period. The simulation (ACTM-W) uses cyclostationary fluxes for the ocean from Takahashi et al. (2009), and for the land from CASA (Randerson et al., 1997). It also uses fossil-fuel fluxes from Jones et al. (2021) which vary both by month and by year. The impact of changing fossil-fuel emissions on MLO SCA is very small (Nevison et al., 2008; Wang et al., 2020). We also found the impact of biomass burning to the MLO SCA is negligibly small in the ACTM simulations.

For the modeled MLO CO_2 time series, we compute SCAs and the growth rate of the amplitude using the same approach as for observations (Section 2.1).

2.3. Climate Data

As in Buermann et al. (2007), we compute 11-year moving-window correlations between MLO SCA and several climate indices to understand which time periods show the strongest correlation. These climate indices include PDO, land temperature, and PDSI, with each time series detrended by removing the long-term linear trend and smoothed by a five-point binomial filter to focus on interannual to decadal variability. The p-value of correlations is computed using 1,000 iterations of 2-tail random phase test (Ebisuzaki, 1997).

The monthly PDO index is provided by National Centers for Environmental Information (NCEI) computed from NOAA's extended reconstruction of SSTs (ERSST Version 5; Huang et al., 2017; Mantua et al., 1997; Zhang

et al., 1997). We compute the annual average PDO as the average of the 12 monthly PDO values for each calendar year.

We use the monthly land temperature data at 1° × 1° spatial resolution provided by Berkeley Earth (Muller et al., 2013). We use the monthly PDSI at 0.5° × 0.5° spatial resolution provided by the Climatic Research Unit (Van Der Schrier et al., 2013). We compute the growing-season average land temperature and PDSI as the average from May to October of each year, and an area-weighted average for Eurasia ($LandT_{EU}$, $PDSI_{EU}$) and North America ($LandT_{NA}$, $PDSI_{NA}$). Eurasia is defined as all land within 30°–70°N and 120°–160°E, while North America is defined as all land between 20°–70°N over the North America land.

We also generate a wind-based climate index, which we call the U-PDO, based on the first EOF of the 700 mbar monthly wind field from NCEP/NCAR within the domain of 10°–40°N and 120°E–100°W (method see Legler, 1983 and Appendix Text S1 in Supporting Information S1). The U-PDO is the *U* wind component (West-East) of this first EOF, as discussed below in Figure 4 and Section 3.3. The choice of 700 mbar is to approximate the pressure level of MLO at ~680 mbar.

2.4. Backward Trajectories

We calculate 10-day back trajectories at MLO using the HYSPLIT program (Draxler & Rolph, 2010; Stein et al., 2015) driven by NCEP/NCAR winds every 6 hr from 1985 to 2019 (Kalnay et al., 1996). The choice of 10-day conforms with prior studies of air-mass originates at MLO (Harris & Kahl, 1990; Harris et al., 1992; Hess, 1996; Miller, 1981). Particles are released at 19.53°N, 155.58°W, and 3,437.00 m.a.s.l. The vertical motion is forced to be along isentropes. All trajectories that reach above 10,000 m altitudes are excluded in our analysis. We compute the fraction of backward trajectories that end above Eurasia or North America on day 10 as a function of the month and the monthly PDO index value.

3. Results

3.1. Observed and Modeled SCA at MLO

In Figure 1a, we show the observed MLO SCA (1960–2019) compared with simulations using Jena-WF. The Jena-WF model approximates the observed variability well (RMSE = 0.27 ppm, $r = 0.86$). Over the whole record from 1959 to 2019, Jena-WF simulates a long-term SCA increase of 0.21 ± 0.040 ppm decade^{-1}, close to the observed increase of 0.22 ± 0.034 ppm decade^{-1}. Jena-WF also captures well the slowing of the SCA growth since the mid-1980s and all-time largest amplitudes around 2015–2017. The simulated growth from 1986 to 2019 is 0.14 ± 0.103 ppm decade^{-1}, compared to 0.16 ± 0.095 ppm decade^{-1} from observations.

In Figure 1b, we show the two components of MLO SCA, one driven by varying winds alone (Jena-W), and one driven by varying ecological CO_2 fluxes alone (Jena-F). Jena-F shows a persistent increase of SCA over time with a growth rate at 0.31 ± 0.024 ppm decade^{-1} over the whole record and 0.29 ± 0.086 ppm decade^{-1} since 1986. In contrast, the Jena-W shows an SCA decrease of −0.10 ± 0.022 ppm decade^{-1} over the whole record, accelerating to −0.15 ± 0.057 ppm decade^{-1} after 1986. In comparison, ACTM-W simulates a relatively smaller SCA decrease of −0.09 ± 0.068 ppm decade^{-1} from 1986 to 2019 (see Table 1, not shown in figure). The growth rate of the SCA trend based on observation, Jena-WF, Jena-W, and ACTM-W is also summarized in Table 1.

In Figure 1c, we show detrended time series for the observations, Jena-WF, Jena-W, and Jena-F, where the detrending involves subtracting a long-term linear trend. Projecting the detrended Jena-W and detrended Jena-F onto the detrended Jena-WF (method see Text S2 in Supporting Information S1), we find the varying winds alone and varying ecological CO_2 fluxes alone play equal roles in driving the SCA variability from 1959 to 2019, accounting for 51% and 49% of the variability, respectively. The SCA variability explained by winds alone increases slightly to 60% during the period from 1986 to 2019.

3.2. Correlation Between MLO CO_2 SCA and Climate Indices

To understand the sources of variability of MLO SCA, we examine the correlation between the observed MLO SCA and a suite of climate indices in Figure 2. This analysis duplicates the method of Buermann et al. (2007), but updates to 2019 and adds PDO and U-PDO to the suite of indices. Over the full record from 1959 to 2019,

Table 1
Observed and Simulated (Jena-WF, Jena-W, and ACTM-W) Long-Term SCA Trends in ppm decade^{-1} at Selected Stations (Methods See Section 2.1)

Stations	Years	SCA trend (ppm decade^{-1})			
		Observation	Jena-WF	Jena-W	ACTM-W
Mauna Loa (MLO, 19.5°N, 155.6°W)	1959–2019	0.22 ± 0.034	0.21 ± 0.040	−0.10 ± 0.022	
	1986–2019	0.16 ± 0.095	0.14 ± 0.103	−0.15 ± 0.057	−0.09 ± 0.068
Barrow (BRW, 71.2°N, 156.4°W)	1961–2019	0.81 ± 0.099	0.83 ± 0.076	0.01 ± 0.054	
	1986–2019	0.96 ± 0.183	0.95 ± 0.156	−0.07 ± 0.127	−0.10 ± 0.206
Midway Island (MID, 27.8°N, 176.7°W)	1986–2019	0.53 ± 0.211	0.21 ± 0.101	−0.10 ± 0.051	−0.05 ± 0.072
Cape Kumukahi (KUM, 19.5°N, 154.8°W)	1976–2019	0.19 ± 0.060	0.18 ± 0.043	−0.08 ± 0.047	
	1986–2019	0.24 ± 0.071	0.19 ± 0.072	−0.10 ± 0.081	−0.05 ± 0.061
Christmas Island (CHR, 2.0°N, 157.3°W)	1975–2019	0.06 ± 0.104	0.05 ± 0.049	−0.06 ± 0.031	
	1986–2019	0.05 ± 0.137	0.02 ± 0.062	−0.04 ± 0.036	−0.01 ± 0.082

Note. Observation data at MLO, BRW, KUM, and CHR are from Scripps CO_2 Program. Observation data at MID are from NOAA ObsPack (Schuldt et al., 2021). Trends are computed using GLS method (see Section 2.1).

the correlation with PDO (r = 0.71, p-value < 0.005) and U-PDO (r = 0.52, p-value < 0.005) are both relatively strong. A marginally significant correlation is also found between MLO SCA and $PDSI_{NA}$ (r = 0.42, p-value = 0.021). There is no significant correlation between MLO SCA and other climate indices ($PDSI_{EU}$, $LandT_{EU}$, and $LandT_{NA}$).

The moving-window correlation with the PDO remains uniformly high ($r \gtrsim 0.5$) throughout the record, except for the period from 1984 to 1995. The correlation with U-PDO shows similar time variations. There is no persistent high correlation between MLO SCA and other climate indices. As noted in Buermann et al. (2007), the correlation between the MLO SCA and $PDSI_{NA}$ increased after the late 1970s, with a high correlation found from 1980 to 1990, from 1995 to 2004. Our analysis also shows that correlation with the $PDSI_{NA}$ is similarly high over the recent period from 2011 to 2019.

3.3. Correlation Between Components of Amplitude Variability and PDSI or PDO

To address whether the SCA-$PDSI_{NA}$ and SCA-PDO correlations are flux-driven or wind-driven, we examine the separate correlations with ACTM-W, Jena-W, and Jena-F, as shown in Figure 3. Each time series is detrended, normalized, and smoothed, using the same method as described in Section 3.2. As shown in Figure 3a, we find a high correlation between PDO and ACTM-W (r = 0.68, p-value = 0.007), and Jena-W (r = 0.73, p-value = 0.008), showing the importance of wind shifts in driving variability in SCA associated with the PDO. The correlation between PDO and Jena-W is stronger since 1980 (r = 0.89, p-value < 0.005). The 11-year moving-window correlation in the lower panel of Figure 3a suggests that the connection between PDO and Jena-W is relatively low before 1977 and around 1990, while the connection between PDO and ACTM-W is relatively low before 1993 and from 2003 to 2009. The PDO index shows a relatively weak correlation between Jena-F at 0.31 (p-value = 0.142), as in Figure 3a. The 11-year moving-window correlation (lower panel of Figure 3a) switches between positive and negative, with a positive high correlation only found around 1975 and since 2008, and a negative high correlation found from 1979 to 1994. Replacing PDO with U-PDO, the moving-window correlations between ACTM-W, Jena-W, and Jena-F are very similar (Figure S1 in Supporting Information S1).

As shown in Figure 3b, we do not find a high correlation between $PDSI_{NA}$ with either Jena-W (r = 0.29, p-value = 0.302) or Jena-F (r = 0.06, p-value = 0.958) over the full record from 1959 to 2018. However, the 11-year moving-window correlation in the bottom panel suggests a relatively tight connection between Jena-W and $PDSI_{NA}$ around 1980, around 1990, from 1995 to 2005, and from 2009 onward. We also find a relatively high correlation between $PDSI_{NA}$ and ACTM-W (r = 0.56, p-value = 0.041) from 1986 to 2018, with a relatively low connection before 1995.

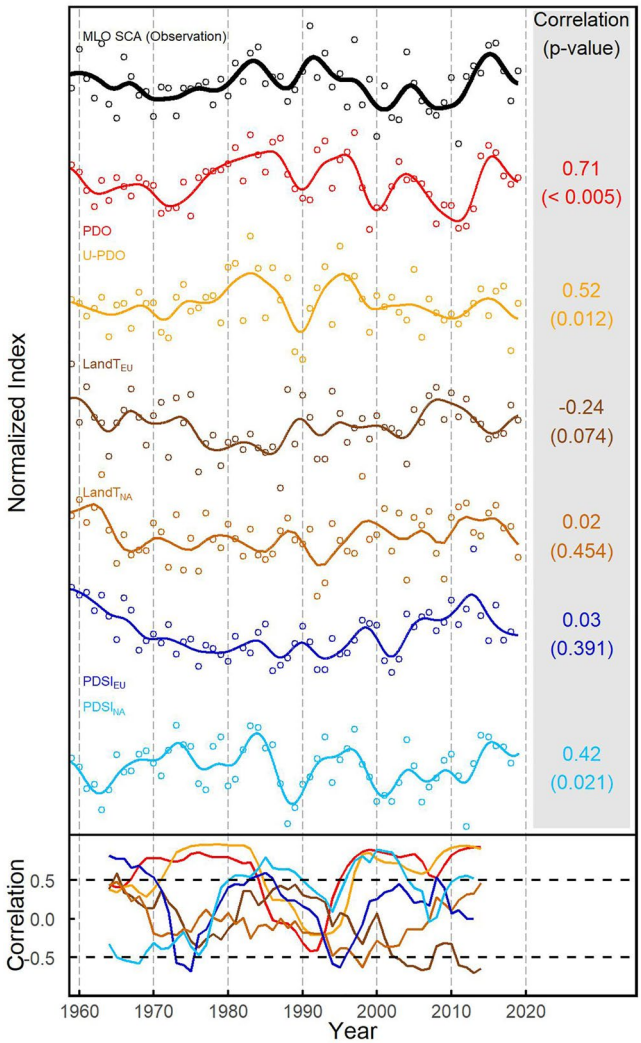

Figure 2. Correlations between Mauna Loa Observatory (MLO) seasonal cycle amplitude (SCA; observation), and various climate indices: annual average Pacific Decadal Oscillation (PDO), annual average U-PDO, annual growing-season (May to October) average land temperature, and PDSI over the Eastern Eurasia ($LandT_{EU}$, $PDSI_{EU}$) and Northern America ($LandT_{NA}$, $PDSI_{NA}$). Eastern Eurasia is defined as 30°–70°N and 120°–160°E over the Eurasia land while North America is defined as 20°–70°N over the North America land. Each time series (points) is first detrended by removing the long-term linear trend and normalized by its standard deviation. We also smooth each time series using a five-point binomial filter, shown as curves. We compute the correlation between each smoothed time series and MLO SCA (observation) in the right of the upper panel, while the *p*-value is computed by 1,000 iterations of two-tailed random phase test (Ebisuzaki, 1997). In the bottom, we show the 11-year moving-window correlation between each smoothed time series and MLO SCA (observation). The moving-window correlations are plotted by using the same color assignments as in the upper panel. The correlation and moving-window correlation between MLO SCA (Observation) and land temperature are computed with land temperature leading by 1 year, following Keeling et al. (1996). Black dashed lines in the lower panel denote the ±0.5 value.

3.4. Large-Scale Wind-Patterns Associated With PDO Variability

To explore the mechanism by which wind shifts impact the MLO SCA variability in association with the PDO, we examine the related U-PDO index, defined based on the first EOF of the Pacific wind field at 700 mbar (Section 2.3). The spatial pattern of the wind EOF is shown in Figure 4a and the temporal variations are shown in Figure 4b. The temporal variation demonstrates a very close association between the U-PDO and the PDO ($r = 0.83$, p-value < 0.005). The high temporal variability of the east-west (U) component of the EOF (i.e., the U-PDO) shows the importance of shifting zonal wind strength in connection with the PDO. When the PDO and U-PDO are positive, a stronger westerly anomaly occurs in the domain from 20°N to 40°N, together with a stronger northerly anomaly in the spatial domain west of 160°E but a stronger southerly anomaly in the spatial domain from 130°W to 160°W. This pattern makes MLO more exposed to air transported from Eurasia in a positive PDO year. We note that, around MLO, the flow pattern shows both western and eastern air-mass origins at all times of a year, but generally progresses from more westerly in winter to easterly in summer (Harris & Kahl, 1990; Harris et al., 1992).

Similar insight is found using HYSPLIT back trajectories at Mauna Loa (Figure 5 and Figure S2 in Supporting Information S1), which show a larger Eurasian footprint and smaller North American footprint associated with positive PDO (Figure 5 and Figure S2 in Supporting Information S1). The back trajectories also resolve seasonality in this pattern. From September to May, the back trajectories favor Eurasian air-mass origins, and from July to August, they favor North American origins. This is true regardless of the phase of the PDO, but the North American influence is strengthened at all seasons during low PDO years, while the Eurasian influence is strengthened from September to May during high PDO years. Analysis of individual back trajectories (Figure S2 in Supporting Information S1) shows that during the winter (DJF) of positive PDO years, most trajectories originate to the west of MLO centered between 20°N and 40°N, suggesting strong zonal flow. In contrast, during the winter of negative PDO years, the trajectories originate over a much wider range of latitudes, both north and south. These winters still have a cluster of trajectories from the west, typically following a curved pathway involving eastward flow at higher latitudes (e.g., 30–50°N) and bending south or southwest on the approach to MLO.

The PDO-related wind shifts are closely associated with the strength of the Aleutian low (Newman et al., 2016), as shown in Figure 6. In a positive PDO year (Figure 6a), the Aleutian low strengthens and moves equatorward, exposing MLO to the influence of westerly winds. In a negative PDO year (Figure 6b), the Aleutian low shrinks and moves poleward, leaving MLO more exposed to air from North America and the eastern Pacific.

4. Discussion

4.1. The Impact of Varying Winds on the SCA Trend

Our analysis allows dividing the observed MLO SCA increase of 0.22 ± 0.034 ppm decade^{-1} ($3.3 \pm 0.51\%$ decade^{-1}) from 1959 to 2019 into components driven by variable winds and variable ecological CO_2 fluxes. From winds alone, we find a decreasing trend of -0.10 ± 0.022 ppm decade^{-1} ($-1.5 \pm 0.33\%$ decade^{-1}) since 1959 based on Jena-W simulations, offsetting ~30% of the increase of $0.22 + 0.10 = 0.3$

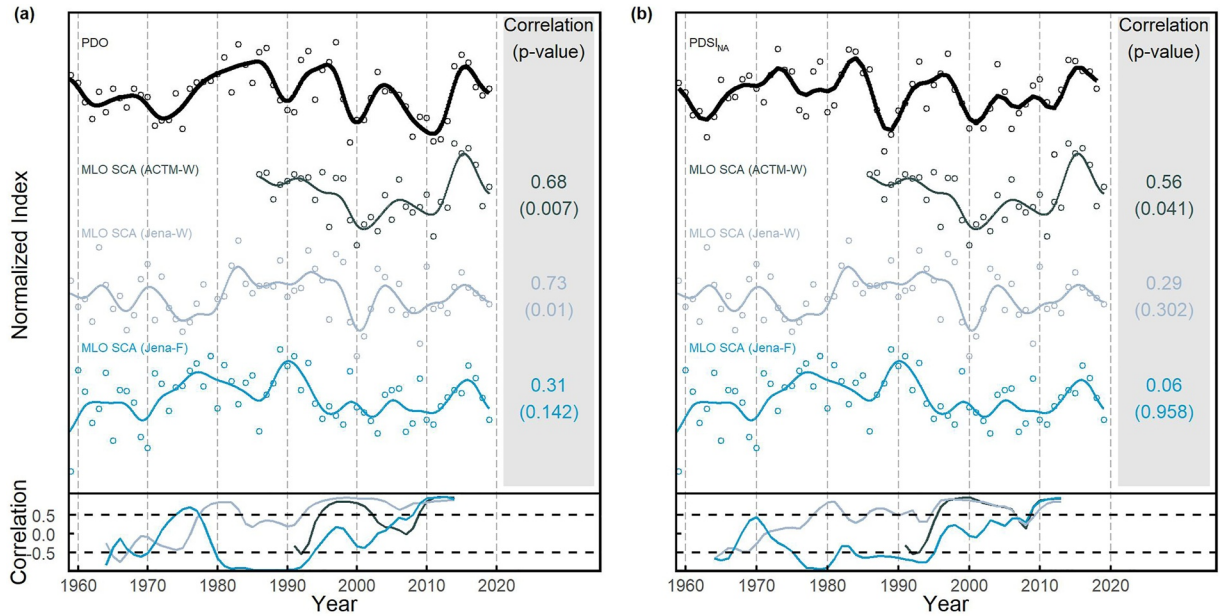

Figure 3. Correlations between (a) annual average Pacific Decadal Oscillation (PDO) or (b) between $PDSI_{NA}$ and various decompositions of the Mauna Loa Observatory (MLO) seasonal cycle amplitude (SCA) variations: modeled MLO SCA from ACTM-W, Jena-W, and Jena-F. Each time series is detrended, normalized, and smoothed using the same method in Figure 2. We compute the correlation between each smoothed time series and the corresponding target (thick black curve) in the right of the upper panel. The target is annual average PDO in (a), and $PDSI_{NA}$ in (b). The *p*-value of the correlation is computed by 1,000 iterations of two-tailed random phase test (Ebisuzaki, 1997). In the bottom panel, we show the 11-year moving-window correlation between each smoothed time series and corresponding target (thick black curve in the upper panel). The moving-window correlations are plotted by using the same color assignments as in the upper. Black dashed lines in the lower panel denote the ±0.5 value.

2 ppm decade^{-1} (4.8% decade^{-1}) expected from ecological flux changes alone. This decreasing trend accelerates to -0.15 ± 0.057 ppm decade^{-1} from 1986 to 2019. Simulations with ACTM-W suggests a slightly smaller decreasing trend (-0.09 ± 0.068 ppm decade^{-1}) from 1986 to 2019. Over the whole record from 1959 to 2019, our results based on Jena-W show a larger wind effect than found by Wang et al. (2020), who suggested a negligibly small overall trend due to changing winds alone. Over the period from 1986 to 2019, the impacts of wind in our study are consistent with Wang et al. (2020), who reported a trend of −0.1 to −0.2 ppm decade^{-1}. This wind impact appears to be an important factor contributing to the relatively smaller SCA increase at MLO (low latitude at 19.5°N) compared to BRW (high latitude at 71.2°N), where Jena-W suggests an insignificant wind-induced trend of 0.01 ± 0.054 ppm decade^{-1} (*p*-value = 0.97 based on Cox-Stuart trend test) from 1961 to 2019. Similarly, ACTM-W suggests an insignificant trend at BRW of -0.07 ± 0.127 ppm decade^{-1} (*p*-value = 0.83 based on Cox-Stuart trend test) from 1986 to 2019, as shown in Table 1. The long-term winds impact at MLO is mostly driven by reduced Eurasia influence, with additional small contributions from reduced North America influence (Figure S3 in Supporting Information S1).

Wind shifts also lead to a smaller SCA at other low-latitude stations, offsetting the observed increases. As shown in Table 1, Jena-W yields similar SCA trends between −0.06 and −0.10 ppm decade^{-1} at the nearby Pacific stations of Midway Island (MID, 27.8°N, 176.7°W) from 1986 to 2019, at Cape Kumukahi (KUM, 19.5°N, 154.8°W) from 1979 to 2019, and at Christmas Island (CHR, 2.0°N, 157.3°W) from 1975 to 2019. Wind shifts thereby offset 16% (at MID), 30% (at KUM), and 50% (at CHR) of the SCA trend expected from ecological flux changes alone. ACTM-W also suggests decreasing SCA from 1986 to 2019 at these three stations, but the magnitude is smaller than that of Jena-W (Table 1). We note that, although Jena-WF underestimated the SCA trend at MID by 50% compared to observation (Table 1), this discrepancy is not necessarily due to error in winds, as it might alternately result from errors in the CO_2 flux fields.

The impact of winds at KUM is of importance in relation to the study of Wenzel et al. (2016), who applied the SCA trend at KUM as an emergent constraint on the magnitude of global CO_2 fertilization effect on gross primary production. However, their study did not evaluate the impact of wind shifts on this constraint.

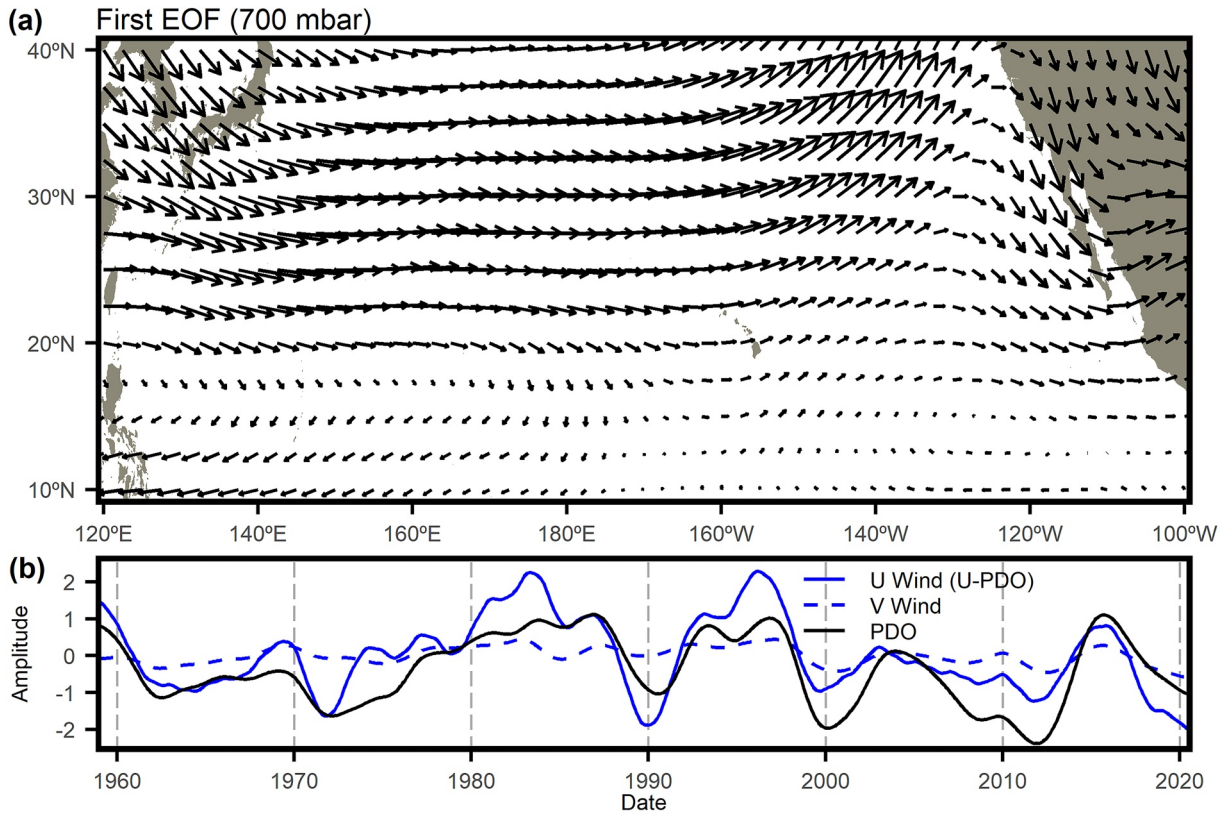

Figure 4. (a) Spatial pattern of the first EOF of 700 mbar monthly average wind (NCEP/NCAR) from 1959 to 2020 within the domain of 10°–40°N and 120°E to 100°W. (b) Temporal pattern of *U* (solid blue, U-PDO) and *V* (dashed blue) winds of the first EOF, and Pacific Decadal Oscillation (PDO; solid black). Each time series with the monthly resolution is smoothed by a five-point binomial filter and normalized by its standard deviation. A positive amplitude of *U* wind temporal pattern represents a stronger westerly anomaly in the domain from 20°N to 40°N, while a positive amplitude of *V* wind temporal pattern represents a stronger northerly anomaly in the spatial domain west of 160°E but a stronger southerly anomaly in the spatial domain from 160°W to 130°W. Normalized monthly PDO (black) smoothed by the same filter are compared here.

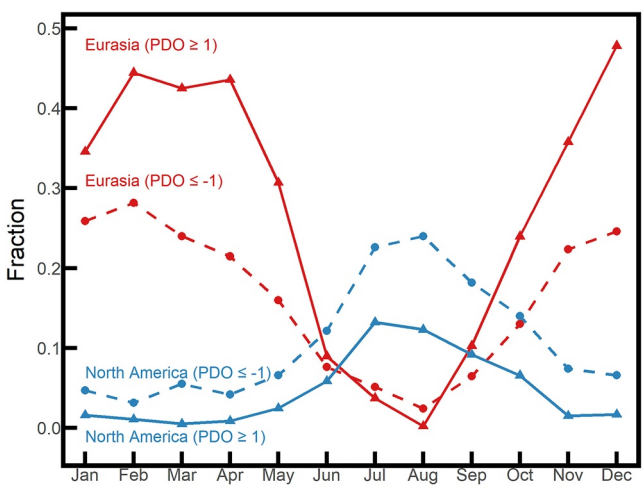

Figure 5. Seasonally varying fraction of Mauna Loa Observatory (MLO) 10-day back trajectories that originate from Eurasia (red) versus North America (blue), sorted by Pacific Decadal Oscillation (PDO) range.

The long-term wind-driven influence on MLO SCA trend and at other stations may have a connection with a poleward shift and weakening of the subtropical jet stream in the Northern Hemisphere (Archer & Caldeira, 2008). This change leads to a weakened influence of fluxes from northern high latitudes of both Eurasia and North America at MLO (Figure S3c in Supporting Information S1). These northern landmasses are the main contributors to the MLO SCA variability and trend (Figure S3b in Supporting Information S1), explaining 58.6% of the total SCA variabilities (method see Text S2 in Supporting Information S1).

The changes of subtropical jet stream are also reflected in the U-PDO index (Figure 4). A notable feature of the U-PDO, which is distinct from the PDO, is a stronger downward trend since 1980, which indicates a progressive weakening of westerly anomalies at 700 mbar within the domain from 20°N to 40°N. To assess the contribution of the U-PDO index to the long-term wind-driven SCA trend since 1980, we use a simple statistical model $\mathrm{SCA(year)} = \alpha \cdot \mathrm{year} + \gamma + \beta \cdot \overline{\mathrm{U-PDO}}\mathrm{(year)}$, where $\overline{\mathrm{U-PDO}}$ is the annual average U-PDO. The parameters are computed using GLS method (similar to Section 2.1). The parameter β (0.21 ± 0.105 ppm U-PDO^{-1}) is largely independent of α, indicated by a negligibly small correlation between β and α ($|r| < 0.05$), and the same model with detrended SCA only leads to a slightly smaller β (0.19 ± 0.132 ppm U-PDO^{-1}). Using $\beta = 0.21$, the trend

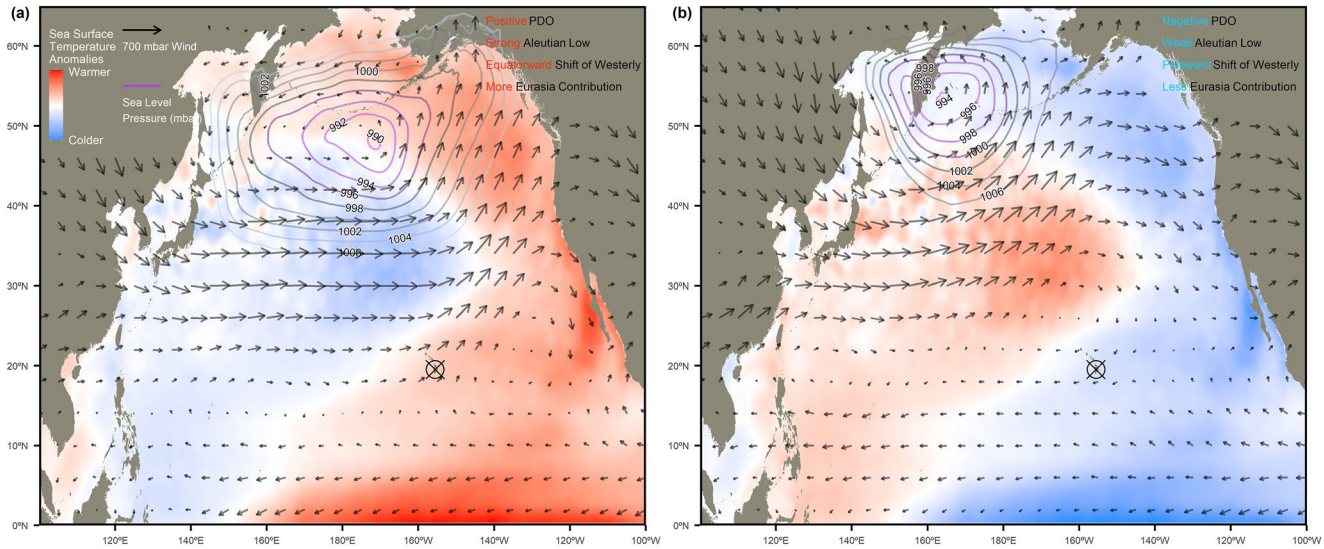

Figure 6. (a) Example of a map of climate variables for a positive Pacific Decadal Oscillation (PDO) year (1997). (b) Example of a map of climate variables for a negative PDO year (2008). The North Pacific sea level pressure and 700 mbar winds (not anomalies) are presented as the January average of the corresponding year, while the sea surface temperature anomaly is presented as the spatial pattern of the first EOF of the monthly Pacific sea surface temperature data from 1980 to 2019. Climate data used here are from MERRA-2 (Gelaro et al., 2017). The location of MLO is marked by the circle cross symbol.

in U-PDO from 1980 to 2019 yields an SCA trend of -0.07 ± 0.032 ppm decade^{-1} which explains ~44% of the full wind-driven effect estimated by Jena-W over this period. Over the full record from 1959 to 2019, the U-PDO term yields an SCA trend of -0.01 ± 0.041 ppm decade^{-1}, which is not significant.

The poleward shift of the subtropical jet stream is possibly tied to a long-term expansion of the Hadley cell. Wang et al. (2020) argued that a southward expansion of the Hadley cell in the Southern Hemisphere made MLO more influenced by CO_2 fluxes from Amazonia, which reduce the CO_2 SCA at MLO because the phase is approximately opposite of the signal from the Northern Hemisphere. Our analysis partly agrees with Wang et al. (2020), but we only find small increasing tropical influence since 2010, as shown in Figure S3 in Supporting Information S1. Here, we suggest that the northward displacement of the northern boundary of the Hadley cell may also have been important (Figure S5 in Supporting Information S1, method see Text S3 in Supporting Information S1 and Adam et al., 2018), associated with northward displacement of Aleutian low under greenhouse warming, corresponding to a wider region of easterly trade winds (Gan et al., 2017; Grise et al., 2019; Staten et al., 2019).

One important caveat in our study is the reliability of winds fields and transport models. The Jena-W (based on TM3 transport model and NCEP reanalysis), the ACTM-W (based on MIROC-ACTM model and JRA-55 reanalysis) simulations and the Wang et al. (2020) study all yield slightly different estimates of the wind impact on the MLO SCA trend from 1986 to 2019 (Table 1). Even larger uncertainties may apply to our estimated trends from 1959 to 2019, which entirely depends on TM3 and NCEP reanalysis. NCEP might have larger errors before the satellite era starting in 1979 (Bromwich & Fogt, 2004). Although climate models and reanalysis products generally show an expanding Hadley cell in the Southern Hemisphere, the similar expansion in the Northern Hemisphere is highly uncertain, with a larger trend from reanalyzes than from model ensemble means (Allen & Kovilakam, 2017; Allen et al., 2014; Grise et al., 2019; Johanson & Fu, 2009; Lu et al., 2007; Staten et al., 2018; Tao et al., 2016).

Will shifting winds continue to contribute to decreasing SCA at low latitudes in the future? The answer may depend on whether the Hadley cell expansion over the past decades has resulted from an internal climate mode or from anthropogenic forcing. This topic remains controversial, with some studies arguing for connection with increasing greenhouse gases (Lu et al., 2007, 2009), and anthropogenic aerosols (Allen & Ajoku, 2016; Allen et al., 2012, 2014), and others pointing to connections with PDO and ENSO indices (Allen & Kovilakam, 2017; Allen et al., 2014; Amaya et al., 2018; Grassi et al., 2012).

4.2. The Impact of Varying Winds on the Variability of MLO SCA

We find that varying winds alone contribute significantly (~51%) to the interannual/decadal variability of MLO SCA. Much of the wind-related variability is tied to the PDO, which modulates the relative impact of Eurasian versus North American influences on the MLO SCA variability. Years with high PDO tend to have large Eurasian influence and larger seasonal cycles. This result is consistent with Lintner et al. (2006), who reported that during the months from April to June (near the seasonal CO_2 peak at MLO), synoptic patterns favoring strong Eurasia influence are associated with high springtime CO_2 anomalies, and patterns favoring North American influence are associated with low springtime CO_2 anomalies. Buermann et al. (2007) similarly attributed part of the long-term MLO SCA decreasing in the early 1990s to the progressively declining Eurasia influence in the northern spring. However, neither of these previous studies noted the close association with the PDO. As shown in Figure S6 in Supporting Information S1, we also find high correlation between MLO SCA and ENSO index (NOAA, 2019) in some periods, but not consistently over the whole period from 1959 to 2019. Lintner et al. (2006) suggested that the connection between SCA and ENSO index can be explained by the flow patterns associated with ENSO phases. This connection can also be tied to the PDO phases, as PDO resembles ENSO on the decadal scale.

We find that the contribution from variations in ecological CO_2 fluxes to the PDO-SCA correlation is small, as indicated by the weak correlation between PDO and Jena-F of 0.33 (Figure 3b). A relatively weak correlation is expected considering that the changes in land temperature or precipitation/evaporation associated with the PDO are quite heterogeneous in space and time (Figure S4 in Supporting Information S1).

Our analysis suggests that the controls of winds on the MLO SCA variability were unusually weak during the period from the mid-1980s to the early 1990s. The SCA was low in the late 1980s and higher in the early 1990s. During the 1985–1995 period, the SCA-PDO correlation (Figure 3a, $r = -0.18$, not smoothed) and the SCA-Jena-W correlation (Figure 1c, $r = -0.03$, not smoothed) was unusually weak, while the SCA-Jena-F correlation was relatively stronger (Figure 1c, $r = 0.45$, not smoothed), suggesting that the variability within this period was dominated by fluxes that were not associated with the PDO. A severe drought in North America in 1988 may have reduced the North American contribution to the SCA variability (Schwalm et al., 2012), while the eruption of the Mt. Pinatubo in 1991 may have strengthened summer CO_2 uptake throughout the Northern Hemisphere (Angert et al., 2004; Gu et al., 2003; Jones & Cox, 2005).

The long-term wind shifts might complicate the attribution of the MLO SCA trend to ecological changes. For example, Buermann et al. (2007) suggested that the decrease or stable SCA trend from 1990 to 2003 was mostly due to more frequent droughts over North America, with additional contributions from wind shifts that led to an overall weakening of springtime Eurasia influence. Our results partially agree with Buermann et al. (2007), as Jena-F driven by midlatitude North America fluxes alone (Figure S3c in Supporting Information S1) shows decreasing SCA anomalies from 1990 to 2000. Over the long-term, however, Jena-F shows North American fluxes contributing to the overall increasing trend in SCA, with this trend persisting after 2000. Also, we do not find a persistent high correlation between $PDSI_{NA}$ and Jena-F, as shown in Figure 3b, but we do find a generally high correlation of $PDSI_{NA}$ with Jena-W since 1980, which is also when $PDSI_{NA}$ show a significant correlation with observed MLO SCA, as in Figure 2. This suggests that the higher PDSI-SCA correlation since the mid-1980s (Figure 2 and in Buermann et al. (2007)) was not driven primarily by CO_2 fluxes tied to drought but rather by wind variability that happens to be correlated with the $PDSI_{NA}$. On the other hand, the $PDSI_{NA}$-Jena-F correlation is high after 2008, possibly implying an increased role of hydrological variability after 2008. More generally, Jena-WF shows that the SCA variability is dominated by the Eurasia influence due to both varying winds and varying ecological CO_2 fluxes, with relatively small contributions from North America (Figure S3b in Supporting Information S1).

5. Summary and Conclusion

We find that varying winds alone contribute significantly to the trend and variability of MLO SCA.

Since 1959, the Jena-W simulations suggest that varying winds by themselves caused a downward SCA trend of -0.10 ± 0.022 ppm decade^{-1}, offsetting ~30% of the long-term SCA increase ($0.22 + 0.1 = 0.32$ ppm decade^{-1}) due to ecological CO_2 flux changes alone. The wind-driven decrease simulated by Jena-W accelerated

after 1986 to -0.15 ± 0.057 ppm decade^{-1}, while this decrease simulated by ACTM-W since 1986 is relatively smaller at -0.09 ± 0.068 ppm decade^{-1}. Both of these two simulations are consistent within uncertainties to Wang et al. (2020), who reported SCA decreasing between -0.1 and -0.2 ppm decade^{-1} driven by changing circulation alone after 1986. Roughly 44% of the post-1980 downward trend is explained by a secular trend of U-PDO (Figure 4b). We also find a wind-driven decreasing tendency in SCA at other low-latitude stations (MID, KUM, and CHR), with Jena-W suggests a larger decrease than ACTM-W (Table 1). Whereas Wang et al. (2020) speculated that the wind effect may be related to Hadley cell expansion in the Southern Hemisphere, we suggest a possibly important role of poleward expansion in the Northern Hemisphere, which acts to isolate the air at low latitudes from the influence of northern high-latitude ecosystems.

On interannual/decadal time scales, we find a high correlation between detrended MLO SCA and the annual average PDO index, as well as a closely related wind index, U-PDO. This high correlation is closely tied to PDO-related wind patterns: (a) In a positive PDO year (Figure 6a), the Aleutian low is stronger and moves equatorward, resulting in a stronger and equatorward-displaced westerly jet over the Pacific which transports air from Eurasia to MLO. (b) In a negative PDO year (Figure 6b), the Aleutian low shrinks and moves poleward and westward, leading to a weaker and poleward-displaced westerly jet, and leaving MLO more exposed to CO_2 transported from North America and the Eastern Pacific.

Our analyses suggest that long-term circulation changes can partly explain the smaller relative SCA growth rate at low latitudes compared to high latitudes, observed at both surface stations and midtroposphere airborne data, as shown in Graven et al. (2013). Especially at low latitudes, the changing circulation makes it hard to simply relate SCA changes to ecological changes, such as the enhanced magnitude of CO_2 fertilization effect (Wenzel et al., 2016) and North America drought (Buermann et al., 2007).

Data Availability Statement

CO_2 observations at MLO, KUM, and CHR are available from the Scripps CO_2 Program at https://scrippsco2.ucsd.edu/ (last access: 15 March 2021). CO_2 observations at MID are provided by the NOAA CML cooperative global air sampling network (CO_2 GLOBALVIEWplus v6.1 ObsPack) and downloaded from http://doi.org/10.25925/20201204 (Schuldt et al., 2021).

The monthly PDO index is provided by National Centers for Environmental Information and downloaded from https://www.ncdc.noaa.gov/teleconnections/pdo/ (last access: 10 April 2021; Huang et al., 2017; Mantua et al., 1997; Zhang et al., 1997). The monthly Oceanic Niño Index (ONI) data are provided by NOAA and downloaded from https://origin.cpc.ncep.noaa.gov/products/analysis_monitoring/ensostuff/ONI_v5.php (last access: 4 January 2022). Land temperature data are provided by Berkeley Earth and downloaded from http://berkeleyearth.lbl.gov/auto/Global/Complete_TAVG_complete.txt (last access: 23 October 2020; Muller et al., 2013). PDSI data are provided by the Climatic Research Unit and downloaded from https://crudata.uea.ac.uk/cru/data/drought/ (last access: 28 August 2020; Van Der Schrier et al., 2013).

Wind data that are used to conduct EOF analysis are from NCEP/NCAR reanalysis and downloaded from https://psl.noaa.gov/data/gridded/data.ncep.reanalysis.pressure.html (last access: 10 December 2020; Kalnay et al., 1996).

Simulated CO_2 time series data based on Jena CO_2 inversion and TM3 transport model, and MIROC-ACTM are available from https://doi.org/10.5281/zenodo.5514400.

Acknowledgments
Y. Jin was supported under a grant from NSF (AGS-1623748) and under a grant from Earth Networks. The historical measurements of the Scripps CO_2 program at MLO, KUM, CHR, BRW, have been supported by numerous grants from NSF and DOE and by staff at the Mauna Loa Observatory, which is supported by NOAA. Recent measurements at these stations have been supported by NASA (NNX17AE74G), NSF (OPP-1304270, OPP-1922922) and by Eric and Wendy Schmidt via recommendation of the Schmidt Futures program, with support for the instrumentation at MLO provided by Earth Networks. We also thank two anonymous reviewers and Dr. Benjamin Lintner for their valuable comments and efforts. Any opinions, findings, conclusions, and recommendations expressed in this material are those of the authors and do not necessarily reflect the views of NSF, NOAA, or DOE.

References

Adam, O., Grise, K. M., Staten, P., Simpson, I. R., Davis, S. M., Davis, N. A., et al. (2018). The TropD software package (v1): Standardized methods for calculating tropical-width diagnostics. *Geoscientific Model Development*, *11*(10), 4339–4357. https://doi.org/10.5194/gmd-11-4339-2018

Allen, R. J., & Ajoku, O. (2016). Future aerosol reductions and widening of the northern tropical belt. *Journal of Geophysical Research: Atmospheres*, *121*, 6765–6786. https://doi.org/10.1002/2016JD024803

Allen, R. J., & Kovilakam, M. (2017). The role of natural climate variability in recent tropical expansion. *Journal of Climate*, *30*(16), 6329–6350. https://doi.org/10.1175/JCLI-D-16-0735.1

Allen, R. J., Norris, J. R., & Kovilakam, M. (2014). Influence of anthropogenic aerosols and the Pacific Decadal Oscillation on tropical belt width. *Nature Geoscience*, *7*, 270–274. https://doi.org/10.1038/ngeo2091

Allen, R. J., Sherwood, S. C., Norris, J. R., & Zender, C. S. (2012). Recent Northern Hemisphere tropical expansion primarily driven by black carbon and tropospheric ozone. *Nature*, *485*, 350–354. https://doi.org/10.1038/nature11097

Amaya, D. J., Siler, N., Xie, S. P., & Miller, A. J. (2018). The interplay of internal and forced modes of Hadley cell expansion: Lessons from the global warming hiatus. *Climate Dynamics*, *51*, 305–319. https://doi.org/10.1007/s00382-017-3921-5

Angert, A., Biraud, S., Bonfils, C., Buermann, W., & Fung, I. (2004). CO_2 seasonality indicates origins of post-Pinatubo sink. *Geophysical Research Letters*, *31*, L11103. https://doi.org/10.1029/2004GL019760

Archer, C. L., & Caldeira, K. (2008). Historical trends in the jet streams. *Geophysical Research Letters*, *35*, L08803. https://doi.org/10.1029/2008GL033614

Bastos, A., Ciais, P., Chevallier, F., Rödenbeck, C., Ballantyne, A. P., Maignan, F., et al. (2019). Contrasting effects of CO_2 fertilization, land-use change and warming on seasonal amplitude of Northern Hemisphere CO_2 exchange. *Atmospheric Chemistry and Physics*, *19*(19), 12361–12375. https://doi.org/10.5194/acp-19-12361-2019

Bromwich, D. H., & Fogt, R. L. (2004). Strong trends in the skill of the ERA-40 and NCEP-NCAR reanalyses in the high and midlatitudes of the Southern Hemisphere, 1958–2001. *Journal of Climate*, *17*(23), 4603–4620. https://doi.org/10.1175/3241.1

Buermann, W., Lintner, B. R., Koven, C. D., Angert, A., Pinzon, J. E., Tucker, C. J., & Fung, I. Y. (2007). The changing carbon cycle at Mauna Loa Observatory. *Proceedings of the National Academy of Sciences of the United States of America*, *104*(11), 4249–4254. https://doi.org/10.1073/pnas.0611224104

Draxler, R. R., & Rolph, G. D. (2010). HYSPLIT (Hybrid Single-Particle Lagrangian Integrated Trajectory) Model access via NOAA ARL READY Website. [Data Set]. NOAA Air Resources Laboratory. Retrieved from http://ready.arl.noaa.gov/HYSPLIT.%20php

Ebisuzaki, W. (1997). A method to estimate the statistical significance of a correlation when the data are serially correlated. *Journal of Climate*, *10*(9), 2147–2153. https://doi.org/10.1175/1520-0442(1997)010<2147:amtets>2.0.co;2.CO;2

Forkel, M., Carvalhais, N., Rödenbeck, C., Keeling, R., Heimann, M., Thonicke, K., et al. (2016). Enhanced seasonal CO_2 exchange caused by amplified plant productivity in northern ecosystems. *Science*, *351*(6274), 696–699. https://doi.org/10.1126/science.aac4971

Fox, J., & Weisberg, S. (2019). *An R companion to applied regression* (3rd ed.).Thousand Oaks, CA: Sage.

Gan, B., Wu, L., Jia, F., Li, S., Cai, W., Nakamura, H., et al. (2017). On the response of the Aleutian low to greenhouse warming. *Journal of Climate*, *30*(10), 3907–3925. https://doi.org/10.1175/JCLI-D-15-0789.1

Gelaro, R., McCarty, W., Suárez, M. J., Todling, R., Molod, A., Takacs, L., et al. (2017). The modern-era retrospective analysis for research and applications, version 2 (MERRA-2). *Journal of Climate*, *30*(14), 5419–5454. https://doi.org/10.1175/JCLI-D-16-0758.1

Grassi, B., Redaelli, G., Canziani, P. O., & Visconti, G. (2012). Effects of the PDO phase on the tropical belt width. *Journal of Climate*, *25*(9), 3282–3290. https://doi.org/10.1175/JCLI-D-11-00244.1

Graven, H. D., Keeling, R. F., Piper, S. C., Patra, P. K., Stephens, B. B., Wofsy, S. C., et al. (2013). Enhanced seasonal exchange of CO_2 by northern ecosystems since 1960. *Science*, *341*(6150), 1085–1089. https://doi.org/10.1126/science.1239207

Gray, J. M., Frolking, S., Kort, E. A., Ray, D. K., Kucharik, C. J., Ramankutty, N., & Friedl, M. A. (2014). Direct human influence on atmospheric CO_2 seasonality from increased cropland productivity. *Nature*, *515*, 398–401. https://doi.org/10.1038/nature13957

Grise, K. M., Davis, S. M., Simpson, I. R., Waugh, D. W., Fu, Q., Allen, R. J., et al. (2019). Recent tropical expansion: Natural variability or forced response? *Journal of Climate*, *32*(5), 1551–1571. https://doi.org/10.1175/JCLI-D-18-0444.1

Gu, L., Baldocchi, D. D., Wofsy, S. C., William Munger, J., Michalsky, J. J., Urbanski, S. P., & Boden, T. A. (2003). Response of a deciduous forest to the Mount Pinatubo eruption: Enhanced photosynthesis. *Science*, *299*(5615), 2035–2038. https://doi.org/10.1126/science.1078366

Harris, J. M., & Kahl, J. D. (1990). A descriptive atmospheric transport climatology for the Mauna Loa Observatory, using clustered trajectories. *Journal of Geophysical Research*, *95*(D9), 13651–13667. https://doi.org/10.1029/JD095iD09p13651

Harris, J. M., Tans, P. P., Dlugokencky, E. J., Masarie, K. A., Lang, P. M., Whittlestone, S., & Steele, L. P. (1992). Variations in atmospheric methane at Mauna Loa Observatory related to long-range transport. *Journal of Geophysical Research*, *97*(D5), 6003–6010. https://doi.org/10.1029/92JD00158

Haverd, V., Smith, B., Canadell, J. G., Cuntz, M., Mikaloff-Fletcher, S., Farquhar, G., et al. (2020). Higher than expected CO_2 fertilization inferred from leaf to global observations. *Global Change Biology*, *26*(4), 2390–2402. https://doi.org/10.1111/gcb.14950

Heimann, M., & Körner, S. (2003). *The global atmospheric tracer model TM3: Model description and user's manual Release 3.8 a*. MPI-BGC.

Hess, P. G. (1996). Trajectories and related variations in the chemical composition of air for the Mauna Loa Observatory during 1991 and 1992. *Journal of Geophysical Research*, *101*(D9), 14543–14568. https://doi.org/10.1029/95JD03611

Higuchi, K., Murayama, S., & Taguchi, S. (2002). Quasi-decadal variation of the atmospheric CO_2 seasonal cycle due to atmospheric circulation changes: 1979–1998. *Geophysical Research Letters*, *29*(8), 1173. https://doi.org/10.1029/2001GL013751

Huang, B., Thorne, P. W., Banzon, V. F., Boyer, T., Chepurin, G., Lawrimore, J. H., et al. (2017). Extended reconstructed sea surface temperature, Version 5 (ERSSTv5): Upgrades, validations, and intercomparisons. *Journal of Climate*, *30*(20), 8179–8205. https://doi.org/10.1175/JCLI-D-16-0836.1

Ito, A., Inatomi, M., Huntzinger, D. N., Schwalm, C., Michalak, A. M., Cook, R., et al. (2016). Decadal trends in the seasonal-cycle amplitude of terrestrial CO_2 exchange resulting from the ensemble of terrestrial biosphere models. *Tellus B: Chemical and Physical Meteorology*, *68*(1), 28968. https://doi.org/10.3402/tellusb.v68.28968

Jiao, W., Wang, L., Smith, W. K., Chang, Q., Wang, H., & D'Odorico, P. (2021). Observed increasing water constraint on vegetation growth over the last three decades. *Nature Communications*, *12*, 3777. https://doi.org/10.1038/s41467-021-24016-9

Johanson, C. M., & Fu, Q. (2009). Hadley cell widening: Model simulations versus observations. *Journal of Climate*, *22*(10), 2713–2725. https://doi.org/10.1175/2008JCLI2620.1

Jones, C. D., & Cox, P. M. (2005). On the significance of atmospheric CO_2 growth rate anomalies in 2002–2003. *Geophysical Research Letters*, *32*, L14816. https://doi.org/10.1029/2005GL023027

Jones, M. W., Andrew, R. M., Peters, G. P., Janssens-Maenhout, G., De-Gol, A. J., Ciais, P., et al. (2021). Gridded fossil CO_2 emissions and related O_2 combustion consistent with national inventories 1959–2018. *Scientific Data*, *8*(1), 2. https://doi.org/10.1038/s41597-020-00779-6

Kalnay, E., Kanamitsu, M., Kistler, R., & Collins, W. (1996). The NCEP/NCAR 40-year reanalysis Project. *Bulletin of the American Meteorological Society*, *77*(3), 437–472. https://doi.org/10.1175/1520-0477(1996)077<0437:tnyrp>2.0.co;2.CO;2

Keeling, C. D. (1960). The concentration and isotopic abundances of carbon dioxide in the atmosphere. *Tellus*, *12*(2), 200–203. https://doi.org/10.1111/j.2153-3490.1960.tb01300.x

Keeling, C. D., Chin, J. F. S., & Whorf, T. P. (1996). Increased activity of northern vegetation inferred from atmospheric CO_2 measurements. *Nature*, *382*, 146–149. https://doi.org/10.1038/382146a0

Keeling, C. D., Piper, S. C., Bacastow, R. B., Wahlen, M., Whorf, T. P., Heimann, M., & Meijer, H. A. (2001). *Exchanges of atmospheric CO_2 and $^{13}CO_2$ with the terrestrial biosphere and oceans from 1978 to 2000. I. Global aspects, SIO Reference Series, No. 01-06* (p. 88). Scripps Institution of Oceanography.

Kobayashi, S., Ota, Y., Harada, Y., Ebita, A., Moriya, M., Onoda, H., et al. (2015). The JRA-55 reanalysis: General specifications and basic characteristics. *Journal of the Meteorological Society of Japan*, *93*(1), 5–48. https://doi.org/10.2151/jmsj.2015-001

Legler, D. M. (1983). Empirical orthogonal function analysis of wind vectors over the tropical Pacific region. *Bulletin of the American Meteorological Society*, *64*(3), 234–241. https://doi.org/10.1175/1520-0477(1983)064<0234:eofaow>2.0.co;2:EOFAOW>2.0.CO;2

Lian, X., Piao, S., Li, L. Z. X., Li, Y., Huntingford, C., Ciais, P., et al. (2020). Summer soil drying exacerbated by earlier spring greening of northern vegetation. *Science Advances*, *6*(1), eaax0255. https://doi.org/10.1126/sciadv.aax0255

Lin, X., Rogers, B. M., Sweeney, C., Chevallier, F., Arshinov, M., & Dlugokencky, E. (2020). Siberian and temperate ecosystems shape Northern Hemisphere atmospheric CO_2 seasonal amplification. *Proceedings of the National Academy of Sciences of the United States of America*, *117*(35), 21079–21087. https://doi.org/10.1073/pnas.1914135117

Lintner, B. R., Buermann, W., Koven, C. D., & Fung, I. Y. (2006). Seasonal circulation and Mauna Loa CO_2 variability. *Journal of Geophysical Research*, *111*, D13104. https://doi.org/10.1029/2005JD006535

Liu, J., Wennberg, P. O., Parazoo, N. C., Yin, Y., & Frankenberg, C. (2020). Observational constraints on the response of high-latitude northern forests to warming. *AGU Advances*, *1*, e2020AV000228. https://doi.org/10.1029/2020AV000228

Lu, J., Deser, C., & Reichler, T. (2009). Cause of the widening of the tropical belt since 1958. *Geophysical Research Letters*, *36*, L03803. https://doi.org/10.1029/2008GL036076

Lu, J., Vecchi, G. A., & Reichler, T. (2007). Expansion of the Hadley cell under global warming. *Geophysical Research Letters*, *34*, L06805. https://doi.org/10.1029/2006GL028443

Mantua, N. J., Hare, S. R., Zhang, Y., Wallace, J. M., & Francis, R. C. (1997). A Pacific interdecadal climate oscillation with impacts on salmon production. *Bulletin of the American Meteorological Society*, *78*(6), 1069–1079. https://doi.org/10.1175/1520-0477(1997)078<1069:apicow>2.0.co;2;2

Miller, J. M. (1981). A five-year climatology of back trajectories from the Mauna Loa Observatory, Hawaii. *Atmospheric Environment (1967)*, *15*(9), 1553–1558. https://doi.org/10.1016/0004-6981(81)90138-4

Muller, R., Rohde, R., Jacobsen, R., Muller, E., & Wickham, C. (2013). A new estimate of the average Earth surface land temperature spanning 1753 to 2011. *Geoinformatics & Geostatistics: An Overview*, *1*(1), 1–7. https://doi.org/10.4172/2327-4581.1000101

Murayama, S., Higuchi, K., & Taguchi, S. (2007). Influence of atmospheric transport on the inter-annual variation of the CO_2 seasonal cycle downward zero-crossing. *Geophysical Research Letters*, *34*, L04811. https://doi.org/10.1029/2006GL028389

Nevison, C. D., Mahowald, N. M., Doney, S. C., Lima, I. D., van der Werf, G. R., Randerson, J. T., et al. (2008). Contribution of ocean, fossil fuel, land biosphere, and biomass burning carbon fluxes to seasonal and interannual variability in atmospheric CO_2. *Journal of Geophysical Research*, *113*, G01010. https://doi.org/10.1029/2007JG000408

Newman, M., Alexander, M. A., Ault, T. R., Cobb, K. M., Deser, C., Di Lorenzo, E., et al. (2016). The Pacific Decadal Oscillation, revisited. *Journal of Climate*, *29*(12), 4399–4427. https://doi.org/10.1175/JCLI-D-15-0508.1

NOAA (National Oceanic and Atmospheric Administration). (2019). Cold and warm episodes by season. [Data Set]. Retrieved from http://origin.cpc.ncep.noaa.gov/products/analysis_monitoring/ensostuff/ONI_v5.php

Patra, P. K., Maksyutov, S., Ishizawa, M., Nakazawa, T., Takahashi, T., & Ukita, J. (2005). Interannual and decadal changes in the sea-air CO_2 flux from atmospheric CO_2 inverse modeling. *Global Biogeochemical Cycles*, *19*, GB4913. https://doi.org/10.1029/2004GB002257

Patra, P. K., Takigawa, M., Watanabe, S., Chandra, N., Ishijima, K., & Yamashita, Y. (2018). Improved chemical tracer simulation by MIROC4.0-based atmospheric chemistry-transport model (MIROC4-ACTM). *Scientific Online Letters on the Atmosphere*, *14*, 91–96. https://doi.org/10.2151/SOLA.2018-016

Peñuelas, J., Ciais, P., Canadell, J. G., Janssens, I. A., Fernández-Martínez, M., Carnicer, J., et al. (2017). Shifting from a fertilization-dominated to a warming-dominated period. *Nature Ecology and Evolution*, *1*, 1438–1445. https://doi.org/10.1038/s41559-017-0274-8

Piao, S., Liu, Z., Wang, Y., Ciais, P., Yao, Y., Peng, S., et al. (2018). On the causes of trends in the seasonal amplitude of atmospheric CO_2. *Global Change Biology*, *24*(2), 608–616. https://doi.org/10.1111/gcb.13909

Pinheiro, J., Bates, D., DebRoy, S., & Sarkar, D. (2021). nlme: Linear and nonlinear mixed effects models. R package version 3.1-152. Retrieved from https://CRAN.R-project.org/package=nlme

Randerson, J. T., Field, C. B., Fung, I. Y., & Tans, P. P. (1999). Increases in early season ecosystem uptake explain recent changes in the seasonal cycle of atmospheric CO_2 at high northern latitudes. *Geophysical Research Letters*, *26*(17), 2765–2768. https://doi.org/10.1029/1999GL900500

Randerson, J. T., Matthew, T. V., Conway, J., Fung, I. Y., & Field, B. (1997). The contribution of terrestrial sources and sinks to trends in the seasonal cycle of atmospheric carbon dioxide. *Global Biogeochemical Cycles*, *11*(4), 535–560. https://doi.org/10.1029/97GB02268

Rödenbeck, C., Houweling, S., Gloor, M., & Heimann, M. (2003). CO_2 flux history 1982–2001 inferred from atmospheric data using a global inversion of atmospheric transport. *Atmospheric Chemistry and Physics*, *3*, 1919–1964. https://doi.org/10.5194/acp-3-1919-2003

Rödenbeck, C., Zaehle, S., Keeling, R., & Heimann, M. (2018). How does the terrestrial carbon exchange respond to interannual climatic variations? A quantification based on atmospheric CO_2 data. *Biogeosciences*, *15*, 2481–2498. https://doi.org/10.5194/bg-2018-34

Schuldt, K. N., Mund, J., Luijkx, I. T., Aalto, T., Abshire, J. B., Aikin, K., et al. (2021). Multi-laboratory compilation of atmospheric carbon dioxide data for the period 1957–2019. [Data Set]. NOAA Global Monitoring Laboratory. https://doi.org/10.25925/20201204

Schwalm, C. R., Williams, C. A., Schaefer, K., Baldocchi, D., Black, T. A., Goldstein, A. H., et al. (2012). Reduction in carbon uptake during turn of the century drought in Western North America. *Nature Geoscience*, *5*, 551–556. https://doi.org/10.1038/ngeo1529

Staten, P. W., Grise, K. M., Davis, S. M., Karnauskas, K., & Davis, N. (2019). Regional widening of tropical overturning: Forced change, natural variability, and recent trends. *Journal of Geophysical Research: Atmospheres*, *124*, 6104–6119. https://doi.org/10.1029/2018JD030100

Staten, P. W., Lu, J., Grise, K. M., Davis, S. M., & Birner, T. (2018). Re-examining tropical expansion. *Nature Climate Change*, *8*, 768–775. https://doi.org/10.1038/s41558-018-0246-2

Stein, A. F., Draxler, R. R., Rolph, G. D., Stunder, B. J. B., Cohen, M. D., & Ngan, F. (2015). NOAA's HYSPLIT atmospheric transport and dispersion modeling system. *Bulletin of the American Meteorological Society*, *96*(12), 2059–2077. https://doi.org/10.1175/BAMS-D-14-00110.1

Taguchi, S., Murayama, S., & Higuchi, K. (2003). Sensitivity of inter-annual variation of CO_2 seasonal cycle at Mauna Loa to atmospheric transport. *Tellus B: Chemical and Physical Meteorology*, *55*(2), 547–554. https://doi.org/10.3402/tellusb.v55i2.16702

Takahashi, T., Sutherland, S. C., Wanninkhof, R., Sweeney, C., Feely, R. A., Chipman, D. W., et al. (2009). Climatological mean and decadal change in surface ocean pCO_2, and net sea-air CO_2 flux over the global oceans. *Deep-Sea Research Part II Topical Studies in Oceanography*, *56*(8–10), 554–577. https://doi.org/10.1016/j.dsr2.2008.12.009

Tao, L., Hu, Y., & Liu, J. (2016). Anthropogenic forcing on the Hadley circulation in CMIP5 simulations. *Climate Dynamics*, *46*, 3337–3350. https://doi.org/10.1007/s00382-015-2772-1

Thomas, R. T., Prentice, I. C., Graven, H., Ciais, P., Fisher, J. B., Hayes, D. J., et al. (2016). Increased light-use efficiency in northern terrestrial ecosystems indicated by CO_2 and greening observations. *Geophysical Research Letters*, *43*, 11339–11349. https://doi.org/10.1002/2016GL070710

Thoning, K. W., Tans, P. P., & Komhyr, W. D. (1989). Atmospheric carbon dioxide at Mauna Loa Observatory 2. Analysis of the NOAA GMCC data, 1974–1985. *Journal of Geophysical Research*, *94*(D6), 8549–8565. https://doi.org/10.1029/JD094iD06p08549

Van Der Schrier, G., Barichivich, J., Briffa, K. R., & Jones, P. D. (2013). A scPDSI-based global data set of dry and wet spells for 1901–2009. *Journal of Geophysical Research: Atmospheres*, *118*, 4025–4048. https://doi.org/10.1002/jgrd.50355

Wang, K., Wang, Y., Wang, X., He, Y., Li, X., Keeling, R. F., et al. (2020). Causes of slowing-down seasonal CO_2 amplitude at Mauna Loa. *Global Change Biology*, *26*(8), 4462–4477. https://doi.org/10.1111/gcb.15162

Wang, T., Liu, D., Piao, S., Wang, Y., Wang, X., Guo, H., et al. (2018). Emerging negative impact of warming on summer carbon uptake in northern ecosystems. *Nature Communications*, *9*(1), 5391. https://doi.org/10.1038/s41467-018-07813-7

Wenzel, S., Cox, P. M., Eyring, V., & Friedlingstein, P. (2016). Projected land photosynthesis constrained by changes in the seasonal cycle of atmospheric CO_2. *Nature*, *538*, 499–501. https://doi.org/10.1038/nature19772

Zeng, N., Zhao, F., Collatz, G. J., Kalnay, E., Salawitch, R. J., West, T. O., & Guanter, L. (2014). Agricultural Green Revolution as a driver of increasing atmospheric CO_2 seasonal amplitude. *Nature*, *515*, 394–397. https://doi.org/10.1038/nature13893

Zhang, Y., Parazoo, N. C., Williams, A. P., Zhou, S., & Gentine, P. (2020). Large and projected strengthening moisture limitation on end-of-season photosynthesis. *Proceedings of the National Academy of Sciences of the United States of America*, *117*(17), 9216–9222. https://doi.org/10.1073/pnas.1914436117

Zhang, Y., Wallace, J. M., & Battisti, D. S. (1997). ENSO-Like interdecadal variability: 1900–93. *Journal of Climate*, *10*(5), 1004–1020. https://doi.org/10.1175/1520-0442(1997)010<1004:eliv>2.0.co;2

Zhao, F., Zeng, N., Asrar, G., Friedlingstein, P., Ito, A., Jain, A., et al. (2016). Role of CO_2, climate and land use in regulating the seasonal amplitude increase of carbon fluxes in terrestrial ecosystems: A multimodel analysis. *Biogeosciences*, *13*(17), 5121–5137. https://doi.org/10.5194/bg-13-5121-2016